Polymer Bulletin (2022) 79:2113–2132
https://doi.org/10.1007/s00289-021-03610-3

ORIGINAL PAPER

Composite filaments OF PHBV reinforced with $ZrO_2 \cdot nH_2O$ particles for 3D printing

Júlia Gomes de Carvalho[1] · Noelle Cardoso Zanini[1] · Amanda Maria Claro[2] · Nayara Cavichiolli do Amaral[2] · Hernane S. Barud[2] · Daniella Regina Mulinari[1]

Received: 30 June 2020 / Revised: 19 January 2021 / Accepted: 23 February 2021 /
Published online: 7 March 2021

Abstract
Fused deposition modeling (FDM) has been a widely applied technology as one of the most practical tools of additive manufacturing in terms of industry 4.0. Biopolymer filaments obtained by extrusion can be a promising material for scaffold manufacturing by FDM 3D printers. In this work, composite filaments of polyhydroxybutyrate-cohydroxyvalerate (PHBV) reinforced with $ZrO_2 \cdot nH_2O$ particles were obtained (1–10% wt/wt.) and characterized aiming the production of scaffolds by FDM process. $ZrO_2 \cdot nH_2O$ particles were prepared and mixed to the PHBV in a mini-extruder. The pristine PHBV and composite filaments (PHBV/ZrO_2) were characterized by stereomicroscopy, scanning electron microscopy (particle analysis), thermogravimetric analysis (TGA and DSC), X-ray diffractometry, Fourier transformed infrared spectroscopy , Vickers microhardness test (HV), and relative density. The addition of $ZrO_2 \cdot nH_2O$ particles altered the behavior of the PHBV matrix: increased the number of $ZrO_2 \cdot nH_2O$ particles in the composite filament surface, enhanced the amorphous phase and the relative density. The PHBV/7.5%ZrO_2 sample presented higher microhardness. It was possible to print the filaments by FDM and the appearance of the scaffolds obtained was a cylindrical structure with rounded inner pores, contributing to the future application in regenerative medicine.

Keywords PHBV · ZrO_2 · NH_2O · Composite filaments · Additive manufacturing (AM) · Scaffolds

✉ Daniella Regina Mulinari
dmulinari@hotmail.com

[1] Universidade do Estado do Rio de Janeiro (UERJ), Rodovia Presidente Dutra km 298, Polo Industrial, Resende, Rio de Janeiro 27537-000, Brazil

[2] Universidade de Araraquara (UNIARA), Rua Carlos Gomes, 1217, São Paulo, Araraquara 14801-320, Brazil

Introduction

Additive manufacturing (AM) has been one of the great intelligent automation technologies that emerged with Industry 4.0, the fourth industrial revolution [1–3], and reached demanding areas of rapid prototyping in product development. The AM, layer by layer, has become consolidated as cost-effective and less resource usage, customization, on-demand, and decentralized production [4]. Besides, AM can be highlighted due to its energy conservation [5] and sustainability due to lower pollutant emissions [6, 7].

As one of many kinds of AM, fused deposition modeling (FDM) is a 3D printing technique based on melting extruded thermoplastic filaments and their deposition of layers [8], the melted and extruded material passes through a nozzle in a heated printer head onto an *x*–*y*–*z*-platform [9], according to pre-set parameters. FDM technique has been attractive for its advantages like common use and availability [10], flexibility, and the ability to build complex parts [11]. Besides, previous studies demonstrated the crescent interest of FDM filament fabrication as an important area [12, 13]. Therefore, with FDM technology, regenerative medicine gained a tool to obtain scaffolds, small three-dimensional structures with interconnected pores, which act as a support for tissue regeneration and can be demonstrated by the literature [14, 15].

Biomaterials can be applied to temporarily support tissue growth [16]. In order to mimic the tissues of a living organism, Diermann et al. [17] mentioned that a scaffold material must be biocompatible, biodegradable, and bioactive (common characteristics of biopolymers and bioceramics). The feasibility of the FDM technique for printing scaffolds can be found in several scientific articles. Choi et al. used poly (lactic acid) (PLA) as extruded filaments to print porous scaffolds by the FDM technique with design freedom as a one-step process [18]. Kovalcik et al. obtained scaffolds by FDM technique from different polyhydroxyalcanoates (PHA's), where polyhydroxybutyrate-cohydroxyvalerate (PHBV) scaffolds stood out for having excellent cell proliferation, nontoxic, with good thermal and mechanical properties [19]. Saska et al. used poly(3-hydroxybutyrate) (PHB) functionalized with osteogenic growth peptide for printing scaffolds by FDM [20]. Ceretti et al. produced multilayered scaffolds of polycaprolactone (PCL) using an open-source FDM printer to study the filament extrusion in the heated print head [14]. Figure 1 evidences the FDM technique of printing a scaffold.

An example of biopolymers with those characteristics had been the PHA's polyhydroxyalcanoates group (PHA's) [21], such as PHB and PHBV for example. Produced from natural resources by bacterial fermentation [22], PHA's are known for having similar properties of low-density polyethylene [23] and good bone regeneration when implanted in an in vivo in bone tissue [24]. Therefore, polyhydroxybutyrate-cohydroxyvalerate (PHBV) biopolymer is an attractive PHA's for medical applications [25], for its biocompatibility properties and good cellular response, as well as its degradation in vivo to hydroxybutyric acid, metabolized by the body [26] although PHBV has shortcomings such as a narrow processing window, expensive, thermal instability, and low impact resistance [25]. Thus,

Fig. 1 FDM printing a scaffold

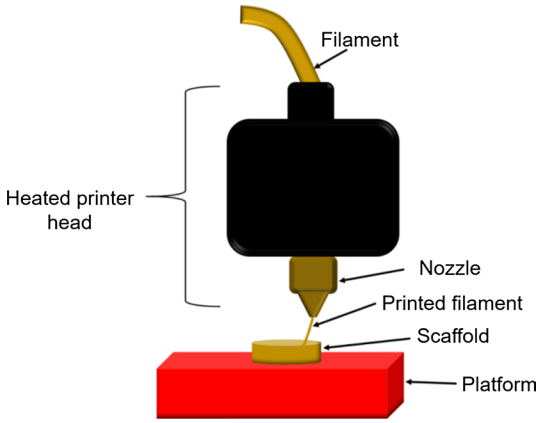

improvement alternatives can solve these drawbacks, such as oxide incorporation in the PHBV matrix or cellulose incorporation, as mentioned in the literature. Shuai et al. proposed the incorporation of zinc oxide in the PHBV matrix to improve its mechanical properties, as well as increasing its crystallinity and its antibacterial character [27]. Rivera-Briso et al. used graphene oxide nanosheets and carbon nanofiber in the PHBV matrix to improve thermal properties, compression characteristics, wettability, and cell proliferation [28]. Augustine et al. incorporated cerium oxide nanoparticles to improve PHBV properties for diabetic wound healing applications [29]. Benini et al. used nanocellulose from pineapple crown in the PHBV matrix and obtained improvements in thermal behavior and crystallinity [30].

Compounds of inorganic oxides have been used to improve polymer properties [31]. Organic–inorganic composite materials and the affinity of the different phases can enhance the polymeric matrix properties. That behavior occurs due to covalent bonds or physical interactions among the organic polymer matrix and inorganic material [23]. In a PHBV matrix, the literature already demonstrated studies with the following reinforcements: zinc oxide [32], silicon dioxide [33], graphite oxide [34], titanium dioxide [35], clay [36], calcium phosphate [37], bioglass [38], attapulgite [39], hydroxyapatite [40], graphene [41], etc. However, there is a lack of studies with PHBV reinforced with zirconium oxide (ZrO_2).

The objective of this research was to develop and characterize PHBV composite filaments reinforced with hydrous zirconium oxide ($ZrO_2{\cdot}nH_2O$) to obtain scaffolds using the FDM 3D printing technique. Zirconium oxide (ZrO_2) is an inorganic material that is an excellent bioceramic due to its good mechanical strength, toughness, chemical stability, biocompatibility, and ability to proliferate osteoblast cells in bone tissue engineering [42]. Da Silva et al. [23] indicated that the addition of ZrO_2 to the polyhydroxybutyrate (PHB) matrix caused thermal and mechanical improvements. Subsequently, $ZrO_2{\cdot}nH_2O$ can also be a good alternative to improve PHBV properties.

The novelty of this work is based on the lack of studies dealing with ZrO_2 as the reinforcement of PHBV biopolymer, especially for applications of FDM filaments

for scaffold manufacturing. There is also a lack of studies with the particle analysis of reinforcements in FDM filaments and studies with Vickers hardness test for FDM filaments. Moreover, the development of filaments encourages the use of the FDM technique, one of the most accessible for manufacturing materials of noble application in tissue engineering.

Materials and method

Materials

With the purpose of obtaining the composite filaments (PHBV/ZrO_2), the PHBV from Biocycle 1000 was supplied by PHB Industrial S/A [43]. PHBV properties provided by the supplier can be seen in Table 1. The $ZrO_2 \cdot nH_2O$ synthesis was according to the method of conventional precipitation described by Mulinari and Da Silva [44].

Preparation of PHBV/ $ZrO_2 \cdot nH_2O$ filaments

Firstly, PHBV dried pellets were mixed with the $ZrO_2 \cdot nH_2O$ (1 to 10% wt/wt). The filaments of PHBV reinforced with different amounts of $ZrO_2 \cdot nH_2O$ (1 to 10% wt/wt) were obtained using a mini-extruder (brand Weellzoom, model B Desktop, Guangdong Prov, China), and the composite samples with $ZrO_2 \cdot nH_2O$ were called PHBV/ X%ZrO_2 where X stands for 1, 2.5, 5, 7.5 and 10% of dispersed $ZrO_2 \cdot nH_2O$.

Characterization PHBV, $ZrO_2 \cdot nH_2O$, and PHBV/ $ZrO_2 \cdot nH_2O$

The morphology of the filaments (pristine PHBV and composites) was investigated by Stereomicroscopy (brand ZEISS, model Axio Imager 2, New York, USA). The microstructure of the filaments (composites and pristine PHBV) and the morphology of the $ZrO_2 \cdot nH_2O$ were also examined by scanning electron microscopy (SEM) microscope (brand HITACHI, Mannheim, Germany), with tungsten filament operating at 5 kV, employing a low-vacuum technique and secondary electron detector. Samples were dispersed on brass support and fixed with a double face 3 M tape. The particle analysis was performed in the images of the filaments by SEM. The ImageJ software measured the diameter of all extruded

Table 1 PHBV Properties

Biopolymer	Lot	PHB (%)	PHB-HV (%)	Melting temperature ($T_{melting}$) (°C)	Molecular mass (MW) (Daltons)	Density (g/cm ^{3})
PHBV	L110	91.93	8.71	167.2	379.160	1.230

filaments and analyzed the $ZrO_2 \cdot nH_2O$ particles on the surface of each composite filament.

Thermal analyses were performed to evaluate the stability of the $ZrO_2 \cdot nH_2O$, pristine PHBV filament, and composite filaments (PHBV/ZrO_2) through a thermogravimetric analyzer (TA Instruments simultaneous TGA/DSC system, model SDT Q600, New Castle, USA). Experiments were carried out under continuous nitrogen flow, with a heating rate of 10 °C min^{-1}, from 30 °C to 600 °C and a specimen weight of 5 mg.

The physical structures of the materials were evaluated by X-ray diffraction (diffractometer Shimadzu Scientific Instruments Incorporated, model XDR-6100, Kyoto, Japan). The measuring conditions were: CuKa radiation with graphite monochromator, 30 kV voltage, and 40 mA electric current. The patterns were obtained in 10–50° angular intervals with 0.05 step and 1 s of counting time.

Micrometer Vickers hardness analysis was performed with a micrometer (HVS Micro Hardness Tester, Hong Kong, China) with a pyramidal diamond tip, on 0.5-mm-thick segments of the material. The material was subjected to indentation with a load of 0.01 mgf/msec and subsequently the indentation area generated for hardness calculation was measured.

The chemical structures of the $ZrO_2 \cdot nH_2O$, pristine PHBV filament, and composite filaments (PHBV/ZrO_2) were analyzed by attenuated total reflectance Fourier transform infrared (ATR-FTIR) spectroscopy (Perkin Elmer® Inc, model Spectrum 100, Massachusetts, USA). The analysis was performed in a transmittance mode, in a range of 4500–400 cm^{-1}, at a resolution of 4 cm^{-1}.

Manufacture of PHBV/ $ZrO_2 \cdot nH_2O$ scaffolds

The pristine PHBV and PHBV/$ZrO_2 \cdot nH_2O$ composite scaffolds (1–7.5% $ZrO_2 \cdot nH_2O$) were designed in TinkerCAD software in cylindrical format and 3D printed using their respective filaments by FDM (GO_3D_S 3D printer, São José dos Campos, Brazil) with 50% filling and processing temperature of ~ 165 °C.

Relative density estimation

Relative density estimation weights and dimensions of the scaffolds (pristine PHBV and PHBV/ $ZrO_2 \cdot nH_2O$ composite scaffolds with 1–7.5% $ZrO_2 \cdot nH_2O$) were measured to calculate their densities. The relative density value of scaffolds (pristine PHBV and PHBV/ $ZrO_2.nH_2O$ composite scaffolds with 1–7.5% $ZrO_2 \cdot nH_2O$) was calculated as Eq. (1) [45]:

$$\rho^* = \frac{\rho_{\text{scaffold}}}{\rho_{\text{solid}}} \tag{1}$$

where ρ_{solid} is the PHBV solid density of 1.23 g/cm^3 (Table 1).

Results

Preparation of PHBV/ $ZrO_2 \cdot nH_2O$ filaments

The processing temperature of the composite filaments (PHBV/ $ZrO_2 \cdot nH_2O$) in the mini-extruder (Fig. 2) was mostly 165 °C (except, PHBV/10% $ZrO_2 \cdot nH_2O$ with 160 °C), slightly lower than the melting temperature ($T_{melting}$) in Table 1 (167.2 °C). The extrusion speed can influence filament linearity [46]. The extrusion speed used to obtain the most linear filaments was 370 mm/min. The extrusion process can be seen in Fig. 2. Geng et al. [46] obtained polyether-ether-ketone (PEEK) filaments analogous to the appearance of the filaments in this research.

Physical–chemical characterization

Figure 3 shows the filaments submitted to the stereomicroscopy technique. It was observed that the filaments did not reveal extreme changes in color except the filaments PHBV/2.5% $ZrO_2 \cdot nH_2O$ and PHBV/10% $ZrO_2 \cdot nH_2O$ (with the highest percentage of oxide), possibly due to the agglomeration of the oxide in the extrusion, also observed by Barbosa and Kenny [47] in polypropylene filaments reinforced with glass fibers. The color change may have been caused by agglomeration but randomly. The process of mixing the reinforcement in the matrix medium may have been insufficient to promote a homogeneous mixture during the extrusion, forming localized parts with a greater amount of oxide than others due to the change in viscosity with the addition of oxide. This fact shows the need for better mixing methods, for better dispersion of the particles. Costa et al. achieved a good dispersion of alumina particles (Al_2O_3) by a thermokinetic mixer that did not compromise the thermal properties of the high-density polyethylene (HDPE) matrix, guaranteeing good mechanical and thermal properties due to

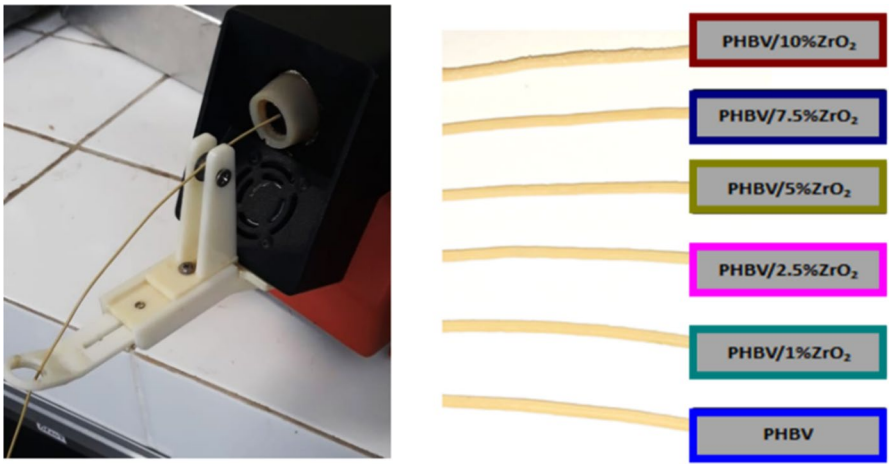

Fig. 2 Filaments extrusion process (left) and photograph images of the all obtained filaments (right)

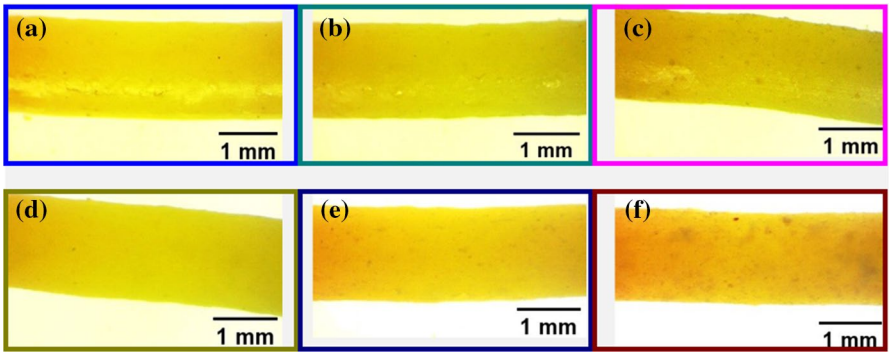

Fig. 3 Stereomicroscopy of the filaments: **a** PHBV; **b** PHBV/1%ZrO_2, **c** PHBV/2.5%ZrO_2, **d** PHBV/5%ZrO_2, **e** PHBV/7.5%ZrO_2 and f) PHBV/10%ZrO_2

good dispersion of the dispersed phase in the composites [48]. The agglomeration might cause an increase in the roughness in the filament surface, making it difficult to slide the filament through the parts of the 3D printer. Lubricants, precise temperature regulation, and extrusion speed control would be needed to improve the surface quality, and possibly contribute to lower mechanical properties [49].

On the other hand, a change was evidenced in the filament microstructures observed by the SEM technique (Fig. 4). The morphology of $ZrO_2{\cdot}nH_2O$ demonstrated the formation of blocks with their agglomerated particles (Fig. 4a–c), which may inhibit the homogenization process between oxide and polymeric matrix, causing defects in the filament. Thus, the addition of oxide in the composition of the filaments was noted whitish points on the surface of the filaments (Fig. 4d–o), also observed by Mallakpour and Ahmadreza [50] in nanocomposites based on modified ZrO_2 nanoparticles and by Bedi, Singh, and Ahuja [51] in recycled LDPE filaments reinforced with SiC/Al_2O_3.

Table 2 reveals the results of the ImageJ analysis by the SEM images. It was observed that the filament diameters were homogeneous, due to the small standard deviation. Compared to the pristine PHBV filament, the diameters of the composite filaments (PHBV/ $ZrO_2{\cdot}nH_2O$) decreased. Besides, all filaments were smaller than the diameter found in standard industrial filaments (1.75 mm) [52]. The analysis of $ZrO_2{\cdot}nH_2O$ particles revealed that there was an increase in the number of particles detected on the filament surface when adding $ZrO_2{\cdot}nH_2O$, as well as an increase in the total area (%) in the image. An effect of particle agglomeration with the addition of $ZrO_2{\cdot}nH_2O$ (also observed by steromicroscopy) can be noted in the increase in measurements referring to the particle perimeter and the particle area. The smallest perimeter measurements were the same, as they reached the minimum size of the program according to the 1 mm scale of the SEM images.

The thermal stability of the pristine PHBV, $ZrO_2{\cdot}nH_2O$, and composite filaments (PHBV/ $ZrO_2{\cdot}nH_2O$) was investigated by thermogravimetric analysis —Fig. 5 shows the TG and DTG results. The curve obtained for pristine PHBV filament and

Fig. 4 SEM of $ZrO_2.nH_2O$ (**a**, **b** and **c**); SEM of the composite filaments: PHBV(**d** and **e**); PHBV/1% ZrO_2(**f** and **g**); PHBV/2.5% ZrO_2(h and i); PHBV/5% ZrO_2 (**j** and **k**); PHBV/7.5% ZrO_2(l and m); PHBV/10%ZrO_2 (**n** and **o**) ▶

composite filaments (PHBV/ $ZrO_2{\cdot}nH_2O$) demonstrated one single event of weight loss in a narrow temperature range attributed to the thermal decomposition of PHBV, demonstrating the remarkable thermal stabilization effect induced by the presence of the $ZrO_2{\cdot}nH_2O$ particles. The TG and DTG curves displayed, respectively, that the degradation T_{onset} and the temperature of the maximum rate of weight loss of the composite filaments (PHBV/ $ZrO_2{\cdot}nH_2O$) with the two highest concentrations of $ZrO_2{\cdot}nH_2O$—notably PHBV/7.5% $ZrO_2{\cdot}nH_2O$ and PHBV/10% $ZrO_2{\cdot}nH_2O$—shifted toward slightly lower temperatures compared to the pristine PHBV filament.

The good dispersion of $ZrO_2{\cdot}nH_2O$ in the matrix and the strong interactions between the two composite components via hydrogen bonding would originate a barrier effect against the transport of decomposition products from the bulk of the matrix to the gas phase, result in enhanced thermal stability for the composites [42]. Besides, a gradual increase in the residue was noted with increasing $ZrO_2{\cdot}nH_2O$ content, indicating that a higher fraction of material did not volatilize upon thermal degradation. Similar thermal behavior was seen by Thiré et al. [39] in nanocomposites based on PHBV and organophilicattapulgite. Table 3 summarizes the results obtained from TG, DTG, and DSC curves.

Figure 6 demonstrates DSC curves for the pristine PHBV filament, $ZrO_2{\cdot}nH_2O$, and composite filaments (PHBV/ $ZrO_2{\cdot}nH_2O$). The values of crystallization temperature (Tc) and crystalline melting temperature (Tm) which are described in Table 3, were obtained from these graphs. The shape of the DSC curves obtained for PHBV filament and $ZrO_2{\cdot}nH_2O$ composites revealed the same profile—the small endothermic peak related to the melting process, indicating that the crystalline structure of both components was maintained. The incorporation of $ZrO_2{\cdot}nH_2O$ decreased the cold crystallization temperature, indicating an enhanced crystallization ability of PHBV. The $ZrO_2{\cdot}nH_2O$ acted as a nucleation agent and induced PHBV crystallization at lower temperatures. A slight increase in melting temperatures was observed with the addition of $ZrO_2{\cdot}nH_2O$ when compared to the pristine PHBV filament; however, the increase of the percentage of $ZrO_2{\cdot}nH_2O$ and nucleate did not have a significant influence on this variation. It is, however, worth mentioning that the presence of the oxide on the studied PHBV composite filaments (PHBV/ $ZrO_2{\cdot}nH_2O$) did not affect the processing and the printing temperature as compared with pristine PHBV since the composites' thermal properties presented similarities. Analogous behavior has been reported by Díez-Pascual and Díez-Vicente [53] to study PHBV composites reinforced with 1, 2, 4, and 8% (wt) of ZnO.

The crystallinity in polymers can affect the mechanical properties [54] and the rate of degradation of the bioresorbable scaffolds (related to water absorption) [55]. In Fig. 7, it was possible to observe the sample diffractograms. The most distinct curve was $ZrO_2{\cdot}nH_2O$ (Fig. 7a), approximating a line due to its amorphous nature, also seen by literature [56].

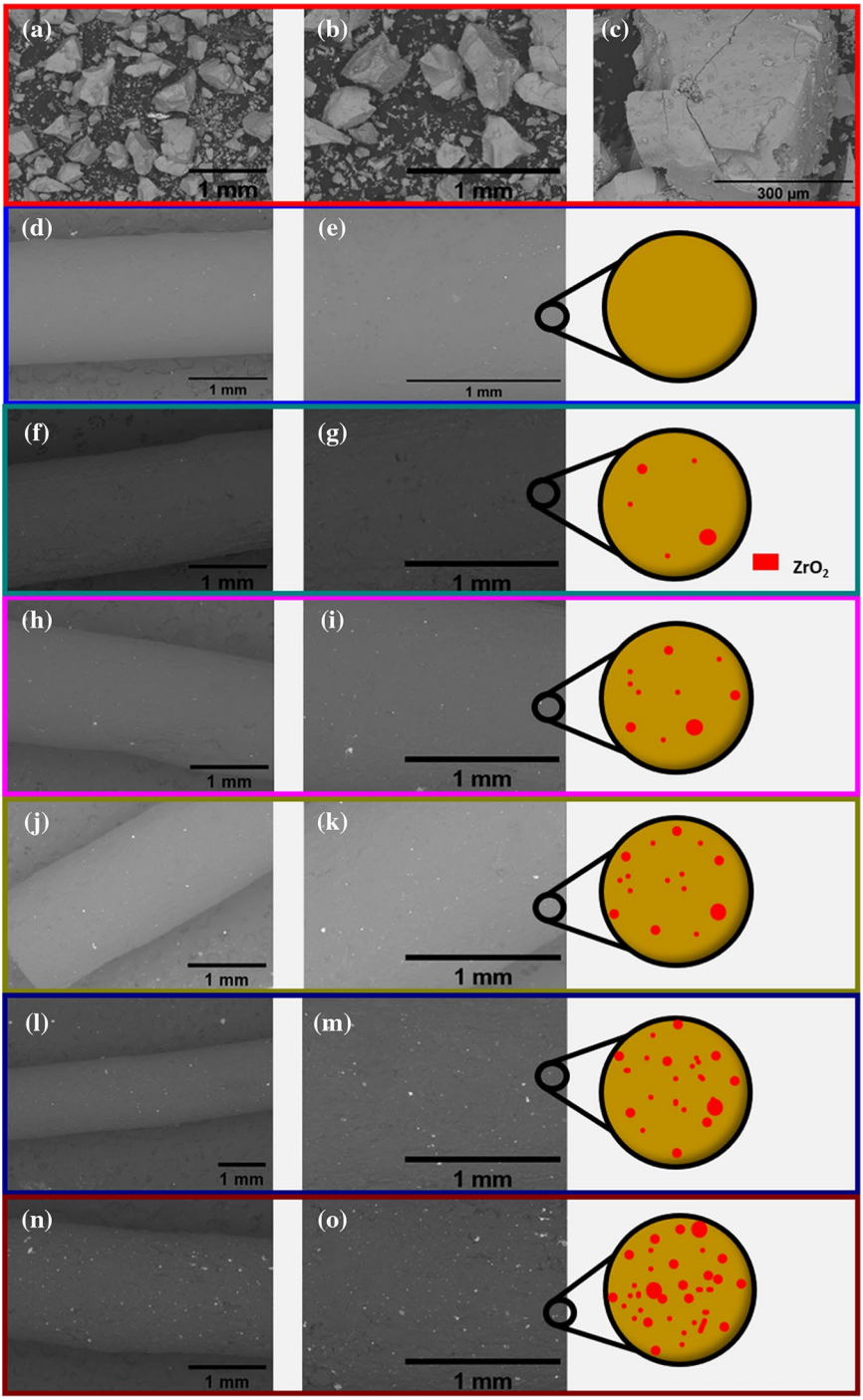
(a)
1 mm
(b)
1 mm
(c)
300 µm
(d)
1 mm
(e)
1 mm
(f)
1 mm
(g)
1 mm
ZrO2
(h)
1 mm
(i)
1 mm
(j)
1 mm
(k)
1 mm
(l)
1 mm
(m)
1 mm
(n)
1 mm
(o)
1 mm

Table 2 Measurement of the diameter of all filaments and analysis of ZrO2 particles from composite filaments using the SEM images

Measurements		PHBV	PHBV/ 1%ZrO_2	PHBV/ 2.5%ZrO_2	PHBV/ 5%ZrO_2	PHBV/ 7.5%ZrO_2	PHBV/ 10%ZrO_2
Filament diameter (mm)		1.59 ± 0.01	1.56 ± 0.01	1.56 ± 0.02	1.47 ± 0.01	1.55 ± 0.01	1.54 ± 0.02
$ZrO_2.nH_2O$ particle analysis	Particles (unit)	–	17	60	97	152	212
	Average area (μm^2)	–	77.6 ± 97.8	90.2 ± 192.8	65.3 ± 106.6	112.9 ± 196.6	75.2 ± 134.1
	The smallest area (μm^2)	–	13.6	13.5	13.0	13.4	12.9
	The biggest area (μm^2)	–	381.3	1000	755.5	2000	1000
	Average perimeter (μm)	–	25 ± 18	27 ± 26	23 ± 16	32 ± 25	27 ± 28
	Smallest perimeter (μm)	–	10	10	10	10	10
	Biggest perimeter (μm)	–	71	186	102	179	249
	Total area in the image (%)	–	0.06	0.25	0.30	0.78	0.93

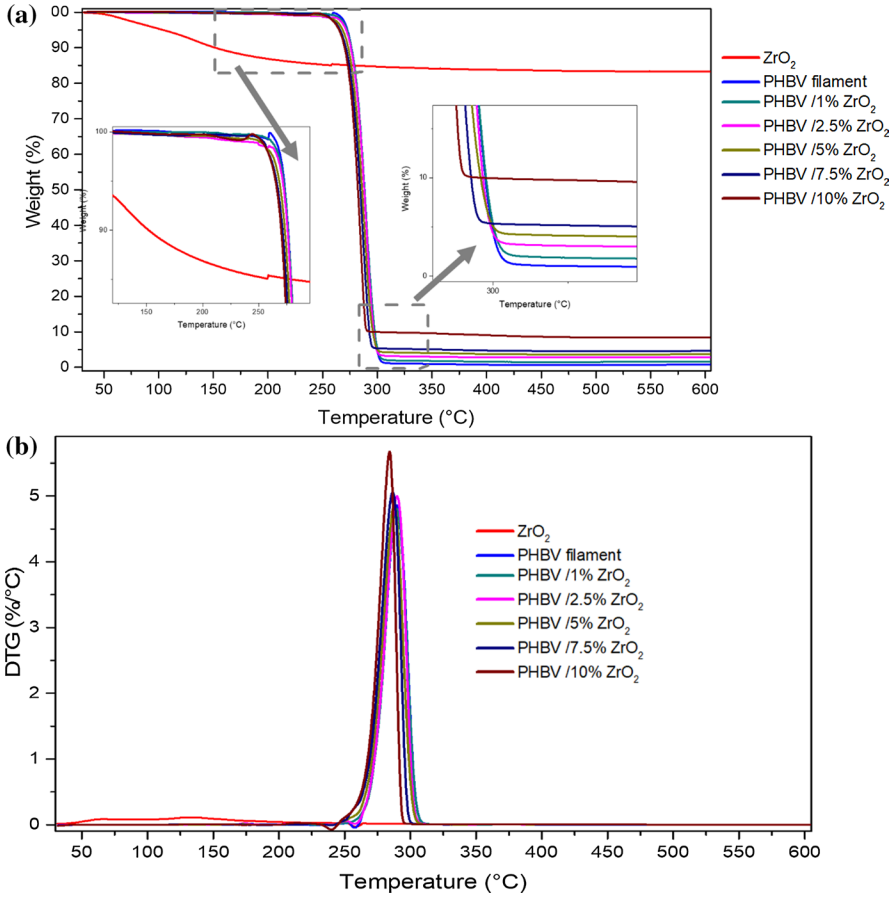

Fig. 5 **a** TG and **b** DTG curves for PHBV filament, $ZrO_2.nH_2O$ and PHBV/ZrO_2 composites

The diffractograms of the PHBV sample revealed characteristic well-defined peaks (2θ) at 13.6°, 17.1°, 21.7°, 22.7°, 25.6° and 30.7°, which correspond to the (020), (110), (101), (111), (121) and (002) reflections of the orthorhombic crystalline lattice, respectively. The diffraction profile of pristine PHBV was equivalent to the PHB homopolymer [57], (Fig. 7c). However, it was noted a decrease in the peaks with $ZrO_2{\cdot}nH_2O$ addition, especially at the peaks of ~ 13.4°, ~ 16.8°, ~ 21.4°; ~ 22.5 °; ~ 25.4°, ~ 27.1° and ~ 30.7º (Fig. 7b and c). Then, the addition of the $ZrO_2{\cdot}nH_2O$ affected the characteristic peaks of PHBV, decreasing the crystallinity of the composites. On the other hand, it can be observed that the peak positions remain practically unchanged in diffractograms of the composite filaments (PHBV/ $ZrO_2{\cdot}nH_2O$). This fact suggests that the pristine PHBV crystalline lattice did not change appreciably in the presence of $ZrO_2{\cdot}nH_2O$. That occurrence can be beneficial for its application in scaffolds, since, their degradation in the bioreabsorption process occurs first

Table 3 TGA and DSC results for PHBV filament, $ZrO_2.nH_2O$ and PHBV/ZrO_2 composites: crystallization temperature (T_c), melting temperature (T_m), onset temperature (T_{onset}) of the degradation process, temperature of maximum rate of weight loss (T_d), mass loss temperature data from TG curves and amount of residue at 600 °C

$ZrO_2.nH_2O$ (wt%)	T_c (ºC)	*T*m (ºC)	T_{onset} (ºC)	T_d (ºC)	Mass loss (%)/ Temp. range (ºC)	Residue (%)
0	48.9	172	278	289	98.5/240–310	0.8
1	46.7	174	278	289	98.0/240–310	1.6
2.5	37.8	174	278	289	95.8/240–310	2.8
5	39.0	175	278	289	95.3/240–310	3.5
7.5	42.7	173	275	286	94.3/240–310	4.6
10	32.4	177	274	284	89.7/240–310	8.4

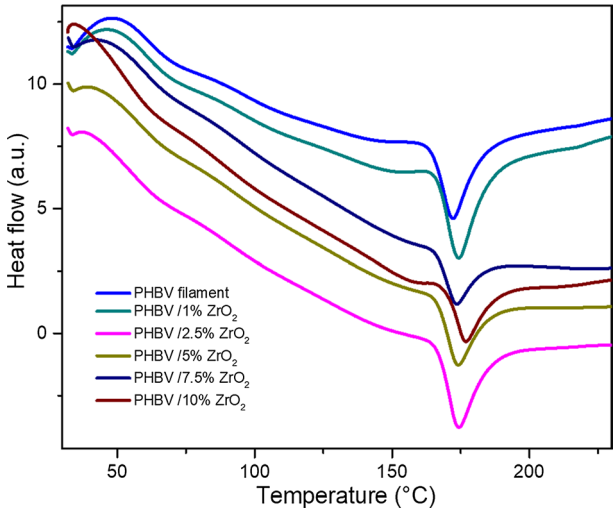

Fig. 6 DSC curves for PHBV filament, $ZrO_2.nH_2O$, and PHBV/ZrO_2 composites

in the water penetrating and diffusing in the amorphous regions of the material, and later in the union of the polymeric chains [55].

Figure 8 reveals the spectra related to the samples analyzed by the FTIR. As can be seen in the XRD, the $ZrO_2{\cdot}nH_2O$ addition to the PHBV matrix affected the behavior of the composite filaments (PHBV/ZrO_2) when compared to the pristine PHBV filament. Most of the characteristic bands of the PHBV matrix decreased after the addition of $ZrO_2{\cdot}nH_2O$ (Fig. 8b–d). The PHBV characteristic bands were (Fig. 8a): the asymmetric stretch of methyl C–H at 2981 cm^{-1}; C–H asymmetric stretching of methylene at 2930 cm^{-1}; C=O stretching band of the ester at 1721 cm^{-1}; absorption band present at 1173 cm^{-1} corresponded to the asymmetric vibration of the C–O–CO (responsible for the bonding of the monomers in the form of polymers with a long chain); folding of the bond in the C=O group at 1459 cm^{-1}; stretch

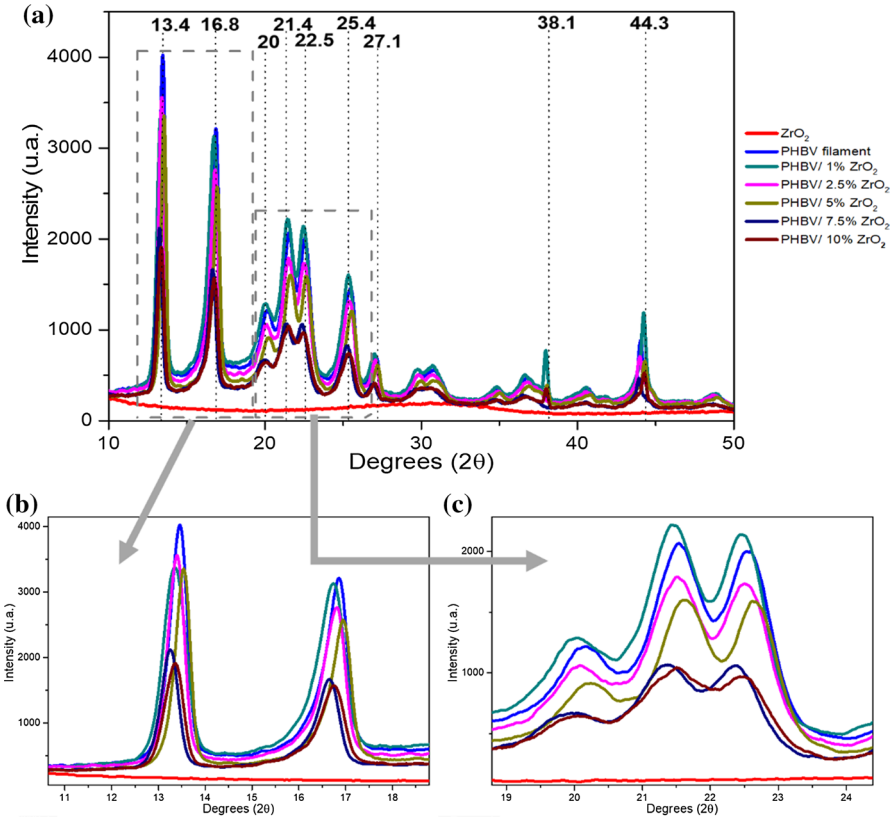

Fig. 7 Diffractograms of the $ZrO_2.nH_2O$, pristine PHBV and composite filaments: **a** range of 10°–50°; **b** zoom corresponding the range of ~ 10° to ~ 19° and **c** zoom corresponding the range of ~ 19° to ~ 24°

in the C–C connection by 979 cm^{-1} [58, 59]. This high-intensity C=O band was attributed to the crystalline form of PHBV. The incorporation of the $ZrO_2{\cdot}nH_2O$ to the PHBV led to a sharp absorption in the wavelengths (absorption maxima in the 3370 – 3390 cm^{-1} region) of the O–H absorption observed for the $ZrO_2{\cdot}nH_2O$. In Fig. 8a was possible to identify the low transmittance bands characteristic of amorphous zirconium oxide: the stretching of hydroxyls for 3228 cm^{-1} band (Fig. 8b) and vibrations of doubling of absorbed H_2O for a 1618 cm^{-1} band (Fig. 8c) [60–62]. The sharp band at 640 cm^{-1} is the characteristic of m-ZrO_2. A broad band around 1500 cm^{-1} is ascribed to Zr-O vibrations of t-ZrO_2 [63].

The hardness of a polymer is related to the critical stress necessary to overcome the cohesive forces of the polymeric chain [64]. For the study of hardness, the strength of the indentation must be analyzed, through the depth of the indentation produced by a material with external penetration [65]. In the case of this work, the Vickers test can be considered a novelty, since there is a lack of researches in literature analyzing Vickers hardness in thermoplastic filaments for 3D application.

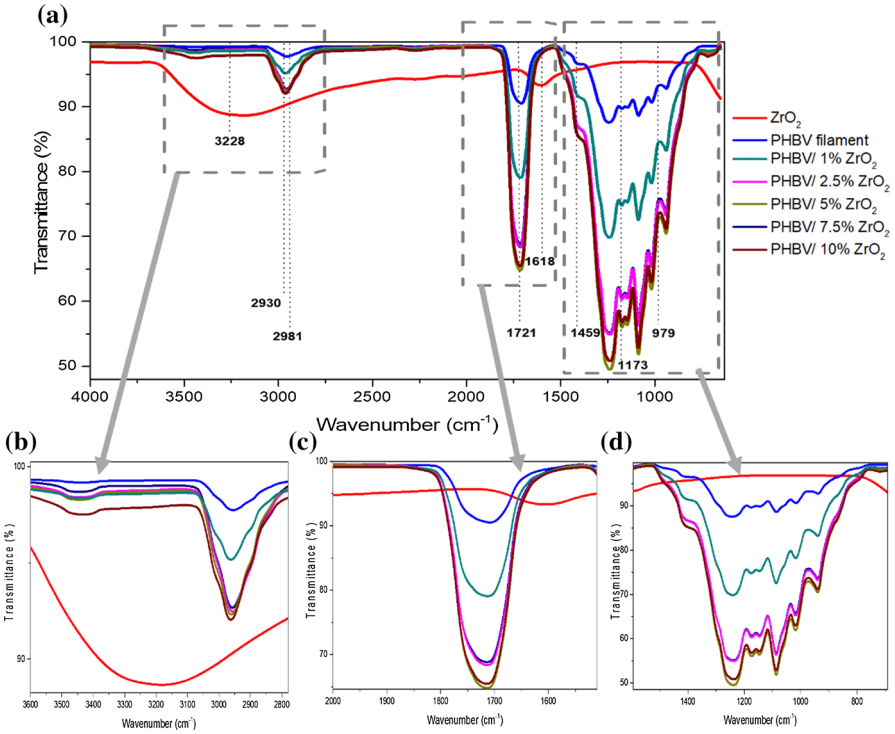

Fig. 8 FTIR spectra of the $ZrO_2.nH_2O$, pristine PHBV, and composite filaments: **a** range of 4000–630 cm^{-1}; **b** zoom corresponding the range of 3600–2800 cm^{-1}; **c** zoom corresponding the range of 2000–500 cm^{-1} and **d** zoom corresponding the range of 1500–630 cm^{-1}

The pristine PHBV (Fig. 9) demonstrated a microhardness value of 105 MPa = 10.7 HV, and an analogous microhardness (13.2 HV) in PHBV composites was found in the literature [66]. As for the composite filaments (PHBV/$ZrO_2{\cdot}nH_2O$), the microhardness values were in the range of 90 to 105 MPa (9.2 to 10.7 HV), similar to pristine PHBV filament. The Vickers microhardness of the composites, tended to decrease with the addition of $ZrO_2{\cdot}nH_2O$, suggesting the presence of microvoids. However, PHBV/7.5% $ZrO_2{\cdot}nH_2O$ had the highest microhardness value (162 MPa = 16.5 HV) and can be promising for scaffold applications in tissue engineering. An analogous microhardness value was found by Ramrakhiani et al. [67], representing a male skull bone (14.7 HV).

In addition to the presence of microvoids influencing the microhardness of the samples, the behavior of PHBV/7.5% $ZrO_2{\cdot}nH_2O$ may be related to the oxide agglomeration during extrusion (as seen in the stereomicroscopy results), compromising reinforcement contents above 7.5% $ZrO_2{\cdot}nH_2O$ and interfering in the composite hardness (making it fragile and mechanically unstable). The microhardness behavior in the PHBV/10% $ZrO_2{\cdot}nH_2O$ can corroborate with the impossibility to print this composite, which will be discussed in the next topic.

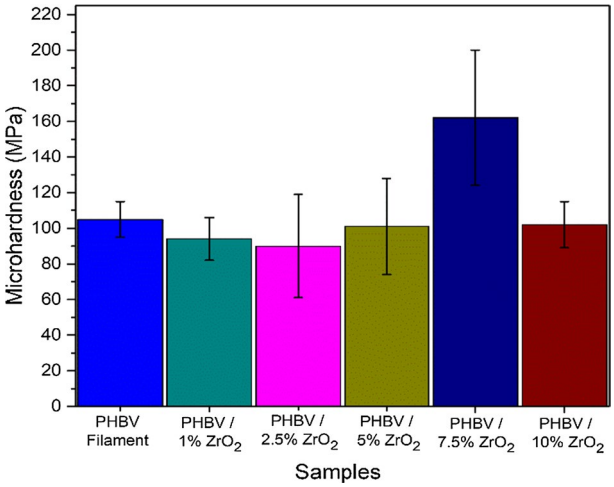

Fig. 9 Microhardness of the composite filaments

Additive manufacture of composite scaffolds PHBV/ $ZrO_2 \cdot nH_2O$ with 1–7.5% $ZrO_2 \cdot nH_2O$

Scaffolds were developed with pristine PHBV filament and composite filaments (PHBV/ZrO_2) from 1 to 7.5% w/w of $ZrO_2 \cdot nH_2O$. The common diameter of a commercial extruded filament for 3D printing is 1.75 mm [52]. From Table 2, it was seen that the filaments obtained in this work did not have values less than 1.47 mm in diameter (with 5% $ZrO_2 \cdot nH_2O$) being 16% smaller than commercial filaments. Although the diameter of the filaments was smaller than industrialized filaments (Table 2) [52], there were no difficulties in printing scaffolds due to this difference. However, the PHBV/10% $ZrO_2 \cdot nH_2O$ was not capable of FDM printing due to the fragility in handling, probably due to the higher oxide load causing particle agglomeration (as seen by SEM and stereomicroscopy). Due to its fragility, the PHBV/10% $ZrO_2 \cdot nH_2O$ composite filament broke when placed in the hole that feeds the FDM printer. In Fig. 10 was possible to notice the appearance of the scaffolds obtained and their cylindrical structure with rounded inner pores. As seen in Fig. 10a, the

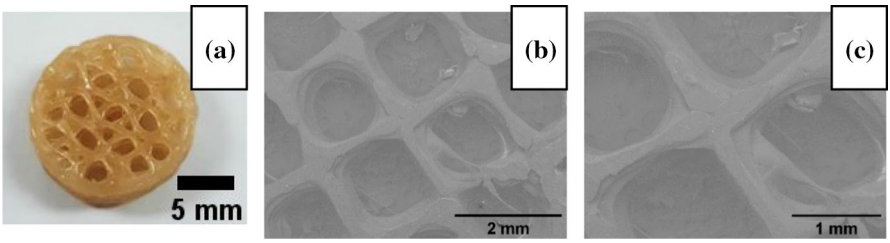

Fig. 10. 3D printed PHBV scaffold (**a**) and SEM images (**b** and **c**)

scaffold obtained was printed with interconnected pores. Figures 10b and c show the SEM images of the scaffolds with regular pores obtained by FDM printing. The literature demonstrated similar scaffolds to the ones obtained by this research [68–72]. The scaffold microstructure can determine its properties and applications [73]. The architecture of a scaffold must mimic the injured area which will be regenerated [74]. Therefore, the porosity of the scaffold is necessary, providing space and supply for cell growth. These pores must be interconnected, so that cell diffusion occurs in the surrounding tissue, as well as the vascularization of the new tissue in development [75].

The diameter of the printed scaffolds did not exceed the measurement of 14.73 mm and its thickness did not exceed the measurement of 4.19 mm (Table 4). The mass of the composites was greater than the pristine PHBV (except for PHBV/7.5% $ZrO_2 \cdot nH_2O$), the same was seen in the density where the boost in density was detected as the proportion of oxide rose (except for 5%).

Conclusion

The overall appearance of the printed composites was acceptable: cylindrical structures and rounder inner pores. For the composite filaments, the addition of $ZrO_2 \cdot nH_2O$ altered the filament behavior when compared with the pristine PHBV filament. SEM analysis showed that the extruded filaments were smaller than the standard industrialized filaments (however it did not affect their 3D printing). Besides, it was observed (by the particle analysis) that with the increase in $ZrO_2 \cdot nH_2O$ to the PHBV, more particles were detected on the filament surface, the larger the area and the perimeter of the filament (due to agglomeration). The amount of $ZrO_2 \cdot nH_2O$ incorporated into the matrix also influenced the thermal properties, a greater amount of residue was observed, and the melting temperature was higher. FT-IR spectra demonstrated that $ZrO_2 \cdot nH_2O$ decreased the characteristic peaks of pristine PHBV in the composite filaments. XRD diffractograms demonstrated that the percentage of $ZrO_2 \cdot nH_2O$ reinforced to the PHBV increased the amorphous phase (possibly facilitating bioreabsoption in its application as a scaffold). PHBV/7.5% $ZrO_2 \cdot nH_2O$ composite filament presented the higher microhardness of them all, assembling to a male skull bone microhardness. As future works, it would be necessary to investigate the characteristics of the printed scaffolds as well as their applications in vitro and in vivo systems.

Table 4 Measurements to find the relative density estimation (ρ^*) of the scaffolds

Scaffold	Diameter (mm)	Thickness (mm)	Mass (g)	$\rho_{scaffold}$ (g/cm^3)	ρ^* (g/cm^3)
Pristine PHBV	14.47	4.19	0.39	0.58	0.47
PHBV/1%ZrO_2	14.31	4.14	0.55	0.84	0.68
PHBV/2.5%ZrO_2	14.34	4.14	0.53	0.80	0.65
PHBV/5% ZrO_2	14.73	4.14	0.53	0.76	0.62
PHBV/7.5% ZrO_2	14.68	4.17	0.36	0.53	0.42

Acknowledgements The authors are grateful for the research support by FAPERJ (process E-26 /260.026/ 2018 and E-26 /010.001800/2015).

References

1. Dilberoglu UM, Gharehpapagh B, Yaman U, Dolen M (2017) The role of additive manufacturing in the era of industry 4.0. Procedia Manuf 11:545–554
2. Haleem A, Javaid M (2019) Additive manufacturing applications in industry 4.0: a review. J Ind Integr Manag. https://doi.org/10.1142/s2424862219300011
3. Kumar A (2018) Methods and materials for smart manufacturing: additive manufacturing, internet of things, flexible sensors and soft robotics. Manuf Lett 15:122–125
4. Niaki MK, Torabi SA, Nonino F (2019) Why manufacturers adopt additive manufacturing technologies: the role of sustainability. J Clean Prod 222:381–392
5. Tang Y, Mak K, Zhao YF (2016) A framework to reduce product environmental impact through design optimization for additive manufacturing. J Clean Prod 137:1560–1572
6. Yang Y, Li L (2018) Total volatile organic compound emission evaluation and control for stereolithography additive manufacturing process. J Clean Prod 170:1268–1278. https://doi.org/10.1016/j.jclepro.2017.09.193
7. Wu CS, Liao HT (2017) Polyester-based green composites for three-dimensional printing strips: preparation, characterization and antibacterial properties. Polym Bull 74:2277–2295. https://doi.org/10.1007/s00289-016-1836-7
8. Gebisa AW, Lemu HG (2018) Investigating effects of Fused-deposition modeling (FDM) processing parameters on flexural properties of ULTEM 9085 using designed experiment. Materials (Basel) 11:1–23. https://doi.org/10.3390/ma11040500
9. Santos-Rosales V, Iglesias-Mejuto A, García-González CA (2020) Solvent-free approaches for the processing of scaffolds in regenerative medicine. Polymers (Basel) 12:533. https://doi.org/10.3390/polym12030533
10. Alafaghani A, Qattawi A, Ablat MA (2017) Design consideration for additive manufacturing: fused deposition modelling. Open J Appl Sci 07:291–318. https://doi.org/10.4236/ojapps.2017.76024
11. Mohamed OA, Masood SH, Bhowmik JL (2016) Optimization of fused deposition modeling process parameters for dimensional accuracy using I-optimality criterion. Meas J Int Meas Confed 81:174–196. https://doi.org/10.1016/j.measurement.2015.12.011
12. Melocchi A, Parietti F, Maroni A et al (2016) Hot-melt extruded filaments based on pharmaceutical grade polymers for 3D printing by fused deposition modeling. Int J Pharm 509:255–263. https://doi.org/10.1016/j.ijpharm.2016.05.036
13. Mohseni M, Hutmacher DW, Castro NJ (2018) Independent evaluation of medical-grade bioresorbable filaments for fused deposition modelling/fused filament fabrication of tissue engineered constructs. Polymers (Basel). https://doi.org/10.3390/polym10010040
14. Ceretti E, Ginestra P, Neto PI et al (2017) Multi-layered scaffolds production via fused deposition modeling (FDM) using an open source 3D printer: process parameters optimization for dimensional accuracy and design reproducibility. Procedia CIRP 65:13–18. https://doi.org/10.1016/j.procir.2017.04.042
15. Ranjan N, Singh R, Ahuja IPS et al (2020) On 3D printed scaffolds for orthopedic tissue engineering applications. SN Appl Sci 2:8–15. https://doi.org/10.1007/s42452-020-1936-8
16. Boonrungsiman S, Thongtham N, Suwantong O et al (2018) An improvement of silk-based scaffold properties using collagen type I for skin tissue engineering applications. Polym Bull 75:685–700. https://doi.org/10.1007/s00289-017-2063-6
17. Diermann SH, Lu M, Dargusch M et al (2019) Akermanite reinforced PHBV scaffolds manufactured using selective laser sintering. J Biomed Mater Res Part B Appl Biomater 107:2596–2610. https://doi.org/10.1002/jbm.b.34349
18. Choi WJ, Hwang KS, Kwon HJ et al (2020) Rapid development of dual porous poly(lactic acid) foam using fused deposition modeling (FDM) 3D printing for medical scaffold application. Mater Sci Eng C 110:110693. https://doi.org/10.1016/j.msec.2020.110693

19. Kovalcik A, Sangroniz L, Kalina M (2020) Properties of scaffolds prepared by fused deposition modeling of poly(hydroxyalkanoates). Int J Biol Macromol 161:364–376
20. Saska S, Pires LC, Cominotte MA (2018) Three-dimensional printing and in vitro evaluation of poly(3-hydroxybutyrate) scaffolds functionalized with osteogenic growth peptide for tissue engineering. Mater Sci Eng C 89:265–273
21. Zubir NHM, Sam ST, Zulkepli NN, Omar MF (2018) The effect of rice straw particulate loading and polyethylene glycol as plasticizer on the properties of polylactic acid/polyhydroxybutyrate-valerate blends. Polym Bull 75:61–76. https://doi.org/10.1007/s00289-017-2018-y
22. Hamour N, Boukerrou A, Djidjelli H, Beaugrand J (2019) In situ grafting effect of a coupling agent on different properties of a poly(3-hydroxybutyrate-co-3-hydroxyvalerate)/olive husk flour composite. Polym Bull 76:6275–6290. https://doi.org/10.1007/s00289-019-02725-y
23. da Silva D da CP, de Menezes LR, da Silva PSRC, Tavares MIB (2019) Evaluation of thermal properties of zirconium–PHB composites. J Therm Anal Calorim. https://doi.org/10.1007/s10973-019-09106-7
24. Dariš B, Knez Ž (2020) Poly(3-hydroxybutyrate): Promising biomaterial for bone tissue engineering. Acta Pharm 70:1–15. https://doi.org/10.2478/acph-2020-0007
25. Muniyasamy S, Ofosu O, Thulasinathan B et al (2019) Thermal-chemical and biodegradation behaviour of alginic acid treated flax fibres/ poly(hydroxybutyrate-co-valerate) PHBV green composites in compost medium. Biocatal Agric Biotechnol 22:101394. https://doi.org/10.1016/j.bcab.2019.101394
26. Kaniuk Ł, Krysiak ZJ, Metwally S, Stachewicz U (2020) Osteoblasts and fibroblasts attachment to poly(3-hydroxybutyric acid-co-3-hydrovaleric acid) (PHBV) film and electrospun scaffolds. Mater Sci Eng C. https://doi.org/10.1016/j.msec.2020.110668
27. Shuai C, Wang C, Qi F et al (2020) Enhanced crystallinity and antibacterial of PHBV scaffolds incorporated with zinc oxide. J Nanomater 2020:6014816. https://doi.org/10.1155/2020/6014816
28. Rivera-Briso AL, Aachmann FL, Moreno-Manzano V, Serrano-Aroca Á (2020) Graphene oxide nanosheets versus carbon nanofibers: enhancement of physical and biological properties of poly(3-hydroxybutyrate-co-3-hydroxyvalerate) films for biomedical applications. Int J Biol Macromol 143:1000–1008
29. Augustine R, Hasan A, Patan NK et al (2020) Cerium oxide nanoparticle incorporated electrospun poly(3-hydroxybutyrate-co-3-hydroxyvalerate) membranes for diabetic wound healing applications. ACS Biomater Sci Eng 6:58–70. https://doi.org/10.1021/acsbiomaterials.8b01352
30. Carvalho Benini KCC de, Ornaghi HL, de Medeiros NM, et al (2020) Thermal characterization and lifetime prediction of the PHBV/nanocellulose biocomposites using different kinetic approaches. Cellulose 27:7503–7522. https://doi.org/10.1007/s10570-020-03318-z
31. Malathi AN, Singh AK (2019) Antimicrobial activity of rice starch based film reinforced with titanium dioxide (TiO 2) Nanoparticles. Agric Res J 56:111. https://doi.org/10.5958/2395-146x.2019.00017.6
32. Anžlovar A, Kržan A, Žagar E (2018) Degradation of PLA/ZnO and PHBV/ZnO composites prepared by melt processing. Arab J Chem 11:343–352. https://doi.org/10.1016/j.arabjc.2017.07.001
33. Han J, Han C, Cao W et al (2012) Preparation and characterization of biodegradable poly(3-hydroxybutyrate-co-4-hydroxybutyrate)/silica nanocomposites. Polym Eng Sci 52:250–258. https://doi.org/10.1002/pen
34. Pramanik N, Bhattacharya S, Rath T et al (2019) Polyhydroxybutyrate-co-hydroxyvalerate copolymer modified graphite oxide based 3D scaffold for tissue engineering application. Mater Sci Eng C 94:534–546. https://doi.org/10.1016/j.msec.2018.10.009
35. Braga NF, Vital DA, Guerrini LM et al (2018) PHBV-TiO2 mats prepared by electrospinning technique: physico-chemical properties and cytocompatibility. Biopolymers 109:1–12. https://doi.org/10.1002/bip.23120
36. da Costa Reis DC, Lemos Morais AC, de Carvalho LH et al (2016) Assessment of the morphology and interaction of PHBV/Clay bionanocomposites: uses as food packaging. Macromol Symp 367:113–118. https://doi.org/10.1002/masy.201500143
37. Das M, Balla V (2015) Additive manufacturing and innovation in materials world. Additive manufacturing. Taylor & Francis, New York, pp 297–332
38. Zhou M, Yu D (2014) Cartilage tissue engineering using PHBV and PHBV/Bioglass scaffolds. Mol Med Rep 10:508–514. https://doi.org/10.3892/mmr.2014.2145

39. Thiré RMDSM, Arruda LC, Barreto LS (2011) Morphology and thermal properties of poly(3-hydroxybutyrate-co-3. hydroxyvalerate)/attapulgite nanocomposites. Mater Res 14:340–344. https://doi.org/10.1590/S1516-14392011005000046
40. Noorani B, Khoshraftar A, Yazdian F et al (2018) Fabrication and evaluation of nanofibrous polyhydroxybutyrate valerate scaffolds containing hydroxyapatite particles for bone tissue engineering. Int J Polym Mater Polym Biomater 67:987–995. https://doi.org/10.1080/00914037.2017.1417283
41. Sridhar V, Lee I, Chun HH, Park H (2013) Graphene reinforced biodegradable poly(3-hydroxybutyrate-co-4-hydroxybutyrate) nano-composites. Express Polym Lett 7:320–328. https://doi.org/10.3144/expresspolymlett.2013.29
42. Bhowmick A, Pramanik N, Jana P et al (2017) Development of bone-like zirconium oxide nanoceramic modified chitosan based porous nanocomposites for biomedical application. Int J Biol Macromol 95:348–356. https://doi.org/10.1016/j.ijbiomac.2016.11.052
43. Benini KCCDC (2015) Compósitos De Nanocelulose / Phbv : Manta. UNESP
44. Mulinari DR, da Silva MLCP (2008) Adsorption of sulphate ions by modification of sugarcane bagasse cellulose. Carbohydr Polym 74:617–620. https://doi.org/10.1016/j.carbpol.2008.04.014
45. Diermann SH, Lu M, Zhao Y et al (2018) Synthesis, microstructure, and mechanical behaviour of a unique porous PHBV scaffold manufactured using selective laser sintering. J Mech Behav Biomed Mater 84:151–160. https://doi.org/10.1016/j.jmbbm.2018.05.007
46. Geng P, Zhao J, Wu W et al (2019) Effects of extrusion speed and printing speed on the 3D printing stability of extruded PEEK filament. J Manuf Process 37:266–273. https://doi.org/10.1016/j.jmapro.2018.11.023
47. Barbosa SE, Kenny JM (2000) Processing of short-fiber reinforced polypropylene. I. Influence of processing conditions on the morphology of extruded filaments. Polym Eng Sci 40:11–22
48. Costa ILM, Zanini NC, Mulinari DR (2020) Thermal and mechanical properties of HDPE reinforced with Al2O3 nanoparticles processed by thermokinectic mixer. J Inorg Organomet Polym Mater. https://doi.org/10.1007/s10904-020-01709-0
49. Kariz M, Sernek M, Obućina M, Kuzman MK (2018) Effect of wood content in FDM filament on properties of 3D printed parts. Mater Today Commun 14:135–140. https://doi.org/10.1016/j.mtcomm.2017.12.016
50. Mallakpour S, Nezamzadeh Ezhieh A (2017) Polymer nanocomposites based on modified ZrO2 NPs and poly(vinyl alcohol)/poly(vinyl pyrrolidone) blend: optical, morphological, and thermal properties. Polym Plast Technol Eng 56:1136–1145. https://doi.org/10.1080/03602559.2016.1253741
51. Bedi P, Singh R, Ahuja IPS (2018) Effect of SiC/Al2O3 particle size reinforcement in recycled LDPE matrix on mechanical properties of FDM feed stock filament. Virtual Phys Prototyp 13:246–254. https://doi.org/10.1080/17452759.2018.1496605
52. Singh AK, Patil B, Hoffmann N et al (2018) Additive manufacturing of syntactic foams: part 1: development, properties, and recycling potential of filaments. Jom 70:303–309. https://doi.org/10.1007/s11837-017-2734-7
53. Díez-Pascual AM, Díez-Vicente AL (2014) ZnO-reinforced poly(3-hydroxybutyrate-co-3-hydroxyvalerate) bionanocomposites with antimicrobial function for food packaging. ACS Appl Mater Interfaces 6:9822–9834. https://doi.org/10.1021/am502261e
54. Shuai C, Yuan X, Yang W et al (2020) Cellulose nanocrystals as biobased nucleation agents in poly-L-lactide scaffold: crystallization behavior and mechanical properties. Polym Test 85:106458. https://doi.org/10.1016/j.polymertesting.2020.106458
55. Olsson DC, Pippi NL, Tognoli GK, Raiser AG (2008) Comportamento biológico de matriz scaffold acrescida de células progenitoras na reparação óssea. Ciência Rural 38:2403–2412
56. Müller D, Heuss-Aßbichler S (2016) Behavior of yttria-stabilized zirconia in the presence of molten salts: part 1 - dissolution and recrystallization phenomena. J Eur Ceram Soc 36:3495–3503. https://doi.org/10.1016/j.jeurceramsoc.2016.05.042
57. Benini KCC d. C, Cioffi MOH, Voorwald HJC (2017) PHBV/cellulose nanofibrils composites obtained by solution casting and electrospinning process. Rev Mater 22:. https://doi.org/https://doi.org/10.1590/s1517-707620170002.0170
58. Perveen K, Masood F, Hameed A (2020) Preparation, characterization and evaluation of antibacterial properties of epirubicin loaded PHB and PHBV nanoparticles. Int J Biol Macromol 144:259–266. https://doi.org/10.1016/j.ijbiomac.2019.12.049

59. Shakil O, Masood F, Yasin T (2017) Characterization of physical and biodegradation properties of poly-3-hydroxybutyrate-co-3-hydroxyvalerate/sepiolite nanocomposites. Mater Sci Eng C 77:173–183. https://doi.org/10.1016/j.msec.2017.03.193
60. Su Y, Cui H, Li Q et al (2013) Strong adsorption of phosphate by amorphous zirconium oxide nanoparticles. Water Res 47:5018–5026. https://doi.org/10.1016/j.watres.2013.05.044
61. Cui H, Li Q, Gao S, Shang JK (2012) Strong adsorption of arsenic species by amorphous zirconium oxide nanoparticles. J Ind Eng Chem 18:1418–1427. https://doi.org/10.1016/j.jiec.2012.01.045
62. Chikere CO, Faisal NH, Kong-Thoo-Lin P, Fernandez C (2020) Interaction between amorphous zirconia nanoparticles and graphite: electrochemical applications for gallic acid sensing using carbon paste electrodes in wine. Nanomaterials 10:537. https://doi.org/10.3390/nano10030537
63. Singh AK, Nakate UT (2014) Microwave synthesis, characterization, and photoluminescence properties of nanocrystalline zirconia. Sci World J. https://doi.org/10.1155/2014/349457
64. Calleja FJB (1985) Microhardness relating to crystalline polymers. Adv Polym Sci. https://doi.org/10.1007/3-540-13779-3_19
65. Pratap B, Gupta RK, Denis L, Goswami D (2020) Evaluation of polymerization shrinkage and vickers hardness for restorative dental composites. Mater Today Proc 21:1563–1565. https://doi.org/10.1016/j.matpr.2019.11.090
66. Batista KC, Silva DAK, Coelho LAF et al (2010) Soil biodegradation of PHBV/Peach palm particles biocomposites. J Polym Environ 18:346–354. https://doi.org/10.1007/s10924-010-0238-4
67. Ramrakhiani M, Pal D, Murty TS (1979) Micro-identation hardness studies on human bones. Cell Tissues Organs 103:358–362
68. Jiang W, Shi J, Li W, Sun K (2012) Morphology, wettability, and mechanical properties of polycaprolactone/hydroxyapatite composite scaffolds with interconnected pore structures fabricated by a mini-deposition system. Polym Eng Sci 52:2396–2402. https://doi.org/10.1002/pen
69. Taboas JM, Maddox RD, Krebsbach PH, Hollister SJ (2003) Indirect solid free form fabrication of local and global porous, biomimetic and composite 3D polymer-ceramic scaffolds. Biomaterials 24:181–194. https://doi.org/10.1016/S0142-9612(02)00276-4
70. Lam CXF, Mo XM, Teoh SH, Hutmacher DW (2002) Scaffold development using 3D printing with a starch-based polymer. Mater Sci Eng C 20:49–56. https://doi.org/10.1016/S0928-4931(02)00012-7
71. Yao Q, Wei B, Guo Y et al (2015) Design, construction and mechanical testing of digital 3D anatomical data-based PCL–HA bone tissue engineering scaffold. J Mater Sci Mater Med. https://doi.org/10.1007/s10856-014-5360-8
72. Thavornyutikarn B, Chantarapanich N, Sitthiseripratip K (2014) Bone tissue engineering scaffolding: computer-aided scaffolding techniques. Progr Biomater 3(2):61–102
73. Wei X, Luo Y, Huang P (2019) 3D bioprinting of alginate scaffolds with controlled micropores by leaching of recrystallized salts. Polym Bull 76:6077–6088. https://doi.org/10.1007/s00289-019-02690-6
74. Andrade GS, Andrade D de B, de Lima GG (2020) TECHNOLOGICAL FORECASTING OF CHITOSAN, SILK FIBROIN AND XANTHAN GUM AS BIOMATERIALS FOR SCAFFOLDS-3D. Rev GEINTEC– ISSN 10:5279–5288. https://doi.org/10.7198/geintec.v10i1.1173
75. Marinho SBN, Gomes D do N, Lima CS de A (2019) Caracterização de scaffold poroso obtido pela técnica de freezecasting. In: Anais do III Simpósio de Inovação em Engenharia Biomédica - SABIO 2019 W. pp 46–43